Draft version June 25, 2017

Preprint typeset using LaTeX style AASTeX6 v. 1.0

HIGH-RESOLUTION NEAR-INFRARED OBSERVATIONS OF A SMALL CLUSTER ASSOCIATED WITH A BRIGHT-RIMMED CLOUD IN W5.

Rieko Imai [1], Koji Sugitani [1], Jingqi Miao [2], Naoya Fukuda [3], Makoto Watanabe [3, 4], Takayoshi Kusune [1] and Andrew J. Pickles [5]

[1]Graduate School of Natural Sciences, Nagoya City University, Mizuho-ku, Nagoya 467-8501, Japan

[2]School of Physical Sciences, University of Kent, Canterbury, Kent CT2 7NR, UK

[3]Okayama University of Science, 1-1 Ridai-chou, Kita-ku, Okayama 700-0005, Japan

[4]Subaru Telescope, National Astronomical Observatory of Japan, 650 North A'ohoku Place, Hilo, HI 96720, USA

[5]Las Cumbres Observatory, Goleta, CA 93117, USA

ABSTRACT

We have carried out near-infrared (IR) observations to examine star formation toward the bright-rimmed cloud SFO 12, of which the main exciting star is O7V star in W5-W. We found a small young stellar object (YSO) cluster of six members embedded in the head of SFO 12 facing its exciting star, aligned along the UV radiation incident direction from the exciting star. We carried out high-resolution near-IR observations with the Subaru adaptive optics (AO) system and revealed that three of the cluster members appear to have circumstellar envelopes, one shows an arm-like structure in its envelope. Our near-IR and L'-band photometry and Spitzer IRAC data suggest that formation of two members at the tip side occurred in advance of other members toward the central part, **under our adopted assumptions.** Our near-IR data and previous

studies imply that more YSOs are distributed in the region just outside the cloud head on the side of the main exciting star, but there is little sign of star formation toward the opposite side. We infer that star formation has been sequentially occurring from the exciting star side to the central part. We examined archival data of far-infrared and CO (J = 3-2) which reveals that, unlike in the optical image, SFO 12 has a head-tail structure which is along the UV incident direction. This suggests that SFO 12 is affected by strong UV from the main exciting star. We discuss the formation of this head-tail structure and star formation there by comparing with a radiation-driven implosion (RDI) model.

1. INTRODUCTION

Bright-rimmed clouds (BRCs) are small molecular clouds located at the edges of evolved H II regions with bright rims facing toward their ionizing stars. They are considered to be the sites for triggered star formation by UV radiation from OB stars. Many theorists consider radiation-driven implosion (RDI) as an efficient way of inducing star formation in such clouds (e.g., Sandford, Whitaker & Klein 1982; Bertoldi 1989; Lefloch & Lazareff 1994; Kessel-Deynet & Burkert 2003; Miao et al. 2009; Gritschneder et al. 2009; Bisbas et al. 2011; Haworth et al. 2012; Kinnear et al. 2014, 2015). Sugitani et al. (1991) and Sugitani & Ogura (1994) cataloged 89 BRCs associated with IRAS point sources as candidate sites for induced star formation, and they classified them into three morphological types of BRCs (type "A"; moderately curved rims, "B"; tightly curved rims, and "C"; cometary rims). These catalogs have stimulated many observations (e.g., Morgan et al. 2004, 2009, 2010; Urquhart et al. 2009; Nakano et al. 2012; Fukuda et al. 2013; Panwar et al. 2014; Kusune et al. 2015). As one such example, Morgan et al. (2008) carried out 450 μm and 850 μm imaging of BRCs in a systematic way using SCUBA on JCMT, and suggested that the bright rim types of B and C represent true "trig-

gered" star formation. Among many examples, only a few ones (Sugitani et al. 1995; Ogura et al. 2002; Ikeda et al. 2008; Matsuyanagi et al. 2006; Choudhury et al. 2010) suggest small-scale sequential star formation from the cloud tip to the center. Although Kessel-Deynet & Burkert (2003) and Bisbas et al. (2011) attempted to explain this sequential star formation by simulations, this mechanism remains incompletely understood and more observational examples are needed.

SFO 12 is a bright-rimmed cloud located in the west of W5 (IC 1848), which is an H II region in the W3/W4/W5 complex and consists of W5-W and W5-E. The bright rim type of this cloud was classified as type B (tightly curved rim; Sugitani et al. 1991) based on its optical shape. The distance range of W5 in the literature is 1.7-2.3 kpc (Sharpless 1955; Johnson et al. 1961; Ishida 1970; Georgelin & Georgelin 1976; Chauhan et al. 2011). In this paper, we adopt the most recent value of 2.2 kpc **for the open cluster IC1848 (Lim et al. 2014) as the distance to SFO12 and its exciting stars in W5-W.** Four O stars (BD +60 586 A, HD 237019, HD 17520 and HD 17505; Koenig et al. 2008) are present in the W5-W and the main exciting star of the bright rim of SFO 12 is BD +60 586 A (O7V; Sota et al. 2011), as seen in Figure 1. The projected distance between SFO 12 and the main exciting star is ∼4.4 pc.

IRAS 02511+6023 is located at the cloud tip and its luminosity was derived as 210 $L_\odot$ at $d = 2.3$ kpc (Carpenter et al. 2000) and 209 $L_\odot$ at $d = 2$ kpc (Karr & Martin 2003) from the IRAS 12-60 μm flux. Morgan et al. (2008) derived the luminosity as 201 $L_\odot$ with $d = 1.9$ kpc and the dust temperature as 21 K. They estimated the cloud mass as 16.87 $M_\odot$ by using this dust temperature. They also derived a spectral type of B7 from the IRAS luminosity. However, because of SFO 12's relatively large distance of ∼2 kpc, there is a need for high-resolution infrared observations to assess the star(s) formed in SFO 12.

First, we examined the global view of SFO 12 in near-infrared (IR) with the University of Hawaii 2.2-m telescope (UH88) located on Mauna Kea Observatory, which is one of the best seeing sites. Then,

we made higher-resolution follow-up observations with the Subaru telescope, where the adaptive optics system was available in the infrared, and used additional optical data we obtained with UH88. Recently, many online/archival data have become available and are provided in an easy to use form. We cross-referenced our detected near-IR sources with online databases of the literature, and used the *Herschel* and JCMT archival data to examine the structure and kinematics of the cloud. Finally, we compared the RDI model with the structure of SFO 12 and discussed triggered star formation there.

In Section 2, we present our optical/near-IR observations and the archival data used here. In Section 3, we describe our photometry results, our derived column density **map**, and CO (J = 3-2) channel maps. In Section 4, we discuss the structure and star formation process of SFO 12.

2. OBSERVATIONS AND ARCHIVAL DATA

2.1. *Optical Observations with the University of Hawaii 2.2 m telescope*

We performed Hα/[SII]/i' imaging on 2009 August 15 and 17 UT with the Wide Field Grism Spectrograph 2 (WFGS2; Uehara et al. 2004) mounted on UH88 to show the positional relation between SFO 12 and its main exciting star, BD +60 586 A, and the distribution of ionized gas around SFO 12 (Figure 1). A 2048 × 2048 pixel Tektronix CCD detector was used. The pixel scale is 0.″34 with a field of view of 11.′5 × 11.′5. Three exposures of 30 s were taken at i'. Four exposures of 180 s were taken at Hα. Three exposures of 300 s were taken at [SII]. The seeing was ∼1.″0 in the i' image. We obtained dome flat frames for flat-fielding.

For i' photometry, we used deeper i'-band images obtained on 2005 November 24 UT. Three 180 s exposures as well as 30 s ones were taken. The SDSS standard star (Hiltner 233; Smith et al. 2002) was observed for photometric calibration at nearly the same airmass as the target. We used IRAF for the data reduction and analysis. The seeing was ∼1.″0 and photometry was performed with an

aperture radius of the seeing size. The limiting magnitude at 0.1 mag error level was ∼21.5.

2.2. *Near-Infrared Observations with the University of Hawaii 2.2 m telescope*

J (1.26 μm), H (1.67 μm), K' (2.11 μm) images of SFO 12 were obtained with the Quick Infrared Camera (QUIRC; Hodapp et al. 1996) mounted on UH88 on 2001 December 25 UT. The QUIRC camera utilizes a 1024 × 1024 pixel HgCdTe array. The pixel scale is 0.″1886 with a field of view of 193″ × 193″. The area of JHK' observation is shown with the dashed box in Figure 1. Nine dithered frames were obtained at each band. The exposure time of each frame was 100 s and the total exposure time was 900 s at each band.

We obtained dome flat frames for flat-fielding and applied sky subtraction with a median self-sky frames. Stellar sources were initially identified by DAOFIND and photometry was performed using PHOT of DAOPHOT with an aperture radius of FWHM size.

The photometric calibration was enforced using the Two Micron All Sky Survey (2MASS) point source catalog (Skrutskie et al. 2006). We used only 2MASS point sources with quality flags of AAA for photometric calibration. The K' filter used has a bandpass very close to that of the 2MASS $K_{\rm s}$ filter, and has been calibrated on $K_{\rm s}$ with no color term. We examined the $J-H$ and $H-K_{\rm s}$ color dependency of the $JHK_{\rm s}$ magnitudes for objects in common between 2MASS and our near-IR photometry. However, no clear dependency was seen, and thus no color correction was applied. The limiting magnitudes at 0.1 mag error level were ∼19.5 at J, ∼18.9 at H, ∼18.3 at $K_{\rm s}$.

2.3. *High-Resolution Near-Infrared Observations with the Subaru telescope*

We obtained higher resolution H, K, L' images of SFO 12 on 2005 August 17 UT by using the Coronagraphic Imager with Adaptive Optics (CIAO; Tamura et al. 2000; Murakawa et al. 2004) mounted on the Subaru telescope. CIAO utilizes a 1024 × 1024 pixel InSb ALADDIN II detector and the field of view is 21.″8 × 21.″8 with a pixel scale of 0.″0213. The Subaru 36-element cassegrain adaptive optics

(AO) system (Takami et al. 1998, 2004) was used. An off-axis guide star (USNO-B 1505-0097752; RA = $02^h54^m57^s.95$, Dec = $60°35'55''.5$;B = 15.67, I = 14.28), which is separated by 30″ from the center of the SFO 12 cluster along the WNW direction, was used for the AO correction. The natural seeing was 0.96″ at R-band at the beginning of the observation. We obtained 21 dithered H frames with a 60 s exposure time, 48 dithered K frames with a 30 s exposure, and 48 dithered L' frames with a 29.7 s coadded exposure time. The total exposure times were 1260 s, 1440 s, and 1425.6 s at H, K, and L', respectively. Photometry was performed with aperture radii of FWHM sizes, 0″.37 in H, 0″.25 in K, and 0″.21 in L'. The UKIRT standard star FS108 was observed for the photometric calibration ($H = 9.765 \pm 0.007$, $K = 9.713 \pm 0.011$, $L' = 9.65 \pm 0.02$) [1]. Twilight frames were taken for flat fielding at H and K-bands. We applied the K-band flat-fielding frame for L'-band flat-fielding.

2.4. *Archival Data*

2.4.1. *Mid-Infrared and CO Data*

We have used the SEIP[2] Source List from the Infrared Array Camera (IRAC; Fazio et al. 2004) of the Spitzer Space Telescope to examine 3.6 μm, 4.5 μm, and 5.8 μm fluxes of each member of a small cluster associated with the head of SFO 12.

The CO (J = 3-2) data cube of the JCMT telescope (JCMTH20080103_00022_01_reduced001_nit_000), was taken from the JCMT Science Archive data[3]. The beam size of JCMT is 14″ at 345 GHz (Buckle et al. 2009) and the frequency interval of this cube is 488 kHz (0.423 km s^{-1} at 345 GHz).

2.4.2. *Column density map from Herschel Data*

We used the *Herschel* Science Archival SPIRE/PACS image data (250 μm from Observation ID: 1342192088, Quality level 2 processed; 160 μm, 100 μm, and 70 μm from Observation IDs:

[1] UKIRT, textfile http://www.ukirt.hawaii.edu/astronomy/calib/phot_cal/faint_stds.html

[2] Spitzer Enhanced Imaging Products http://irsa.ipac.caltech.edu/cgi-bin/Gator/nph-scan?projshort=SPITZER

[3] JCMT Science Archive data http://www.cadc-ccda.hia-iha.nrc-cnrc.gc.ca/en/search/

1342217393/1342217394 and 1342191006/1342191007, Quality level 2.5 processed) to make dust temperature (T_d) and column density maps in a similar way of Konyves et al. (2010).

First, we convolved the shorter wavelength *Herschel* images to the resolution (18″) of the 250 μm image by using the IDL package developed by Aniano et al. (2011). Then, we resampled down the shorter wavelength images to the the same grid size of the the 250 μm image (6″) and derived spectral energy distributions (SED) at each position of the 250 μm image. Here, we adopted the area of $\sim$1.′5 $\times$ 1.′5, centered at (RA, Dec)$_{\rm J2000}$ = ($2^{\rm h}59^{\rm m}27^{\rm s}$, +60°22′26″), as an area of the zero point of the surface brightness for SFO 12 cloud.

Assuming a single temperature of dust emission, a gray-body SED fitting was performed with a function of $I_\nu = B_\nu(T_D)(1 - e^{\tau_\nu})$, where B_ν is the Planck function, I_ν is the observed surface brightness at frequency ν, $\tau_\nu = k_\nu \Sigma$ is the dust opacity, and k_ν is the dust opacity per unit mass. We adopted $k_\nu = 0.1\ (\nu\ /\ 1000\ {\rm GHz})^\beta\ {\rm cm^2\ g^{-1}}$ and $\beta = 2$ (Konyves et al. 2010). As the data weight of SED fitting, we adopted $1/\sigma^2$, where σ^2 is the square sum of the rms noise and the calibration uncertainties of surface brightnesses (15% at 250 μm; Griffin et al. 2010, 20% at 160 μm and 10% at 100/70 μm; Poglitsch et al. 2010).

3. RESULTS

3.1. *JHK′ imaging*

Figure 2 shows a three-color composite image made by the J, H, and K' data of UH88. The bright rim seen in the optical image (Figure 1) can be also identified in this composite image. A small cluster is clearly seen in the infrared image towards the region enclosed by the bright rim; it appears to consist of six sources. This cluster cannot be identified in the optical image **and the photometry results of the cluster members are presented in Table 1.** The position of IRAS 02511+6023 agrees with that of this cluster within its positional error, and we conclude the IRAS

source corresponds to this cluster embedded in SFO 12.

3.2. *High-Resolution HKL' imaging*

We show high-resolution HKL' images toward the cluster of SFO 12 in Figure 3. The areas of the H and K images correspond with the dashed-line box in Figure 2, but the L' image is slightly smaller than that box. The six cluster members mentioned above are clearly separated in the H and K images, and we refer to these sources as S1-S6 (see Figure 3). In the L' image, while S1 and S2 cannot be identified, S3-S6 are clearly detected. **The photometry results with Subaru are presented in Table 2.** The distribution of the cluster members is not symmetric, and elongated. **The elongated direction determined by simple, linear fitting for the member's positions is PA=**$124^\circ \pm 10^\circ$, nearly the same as the UV incident direction from the main exciting star **to the position center of the cluster, PA**$\sim 118^\circ$**, where their coordinates presented in Table 1 are used.**

Nebulosities can be clearly identified around S1, S2, and S4 (Figure 3b). We examined their close-up images to determine the details of these sources (Figures 4, 5, and 6). Additionally we examined the other cluster members and found that S3 is likely a binary star (Figure 7) while S5 and S6 seem to be single stars.

S1 seems to be a single star with an envelope that reflects the light from itself (Figure 4). This envelope can be also recognized in the non-AO image of UH88 (Figure 2). This envelope appears to have a size of ∼2000-3000 AU and strongly suggests its youth.

Figure 5a shows that S2 is a binary system, and Figure 5b clearly shows an arm-like feature extending from S2 in its circum-binary envelope. This arm-like feature may consist of two arms although their separation cannot be clearly realized in Figure 5b. The size of this feature is ∼4000 AU (Figure 5b). This arm-like system appears to be similar to the results of the self-gravitational hydrodynam-

ical numerical simulations, for multiple star system with arm-like features (e.g., Matsumoto et al. 2015).

The nebulosity shape and peak intensity position of S4 differ at H, K, and L' images (Figure 6a-c). We made a composite image of H, K, and L' to clearly show these differences (Figure 6d). The cross shows the peak intensity position at L'. The distance of the peak position from the cross position increases with the decreasing wavelengths from L' to H, and the cone-shaped nebulosity is more extended at H than K while it cannot be seen at L'. This situation suggests that we view S4 nearly edge-on, like protostellar envelope models (e.g., Figure 12a of Whitney et al. 2003).

Because S3, which is the most luminous among the cluster members, appears to have a companion star (Figure 7a), we tried to subtract the main stellar component of S3 (S3a). We roughly scaled the intensity of S5 to that of S3, and subtracted the scaled image from the S3 image (Figure 7b). Figure 7b clearly shows the companion star (S3b). The projected separation between the main star and the companion is ∼2000 AU.

3.3. *Photometric properties of YSO candidates*

In addition to the cluster members, we searched for more YSO candidates around SFO 12 using our UH88 photometric data. We constructed a $J-H$ versus $H-K_s$ diagram to identify near-IR excess sources as YSO candidates (Figure 8). Only the sources detected with photometric errors <0.1 mag in 3 bands were used for plotting, except for the cluster members. Ten sources are located redward of the reddening line from the A0 star and are **indicated** by magenta filled circles **with ID numbers** in Figure 8, corresponding to their locations **marked by magenta-colored numbers** in Figure 2.

In order to exclude distant galaxies, we also constructed a $J-K_s$ versus $i'-J$ diagram **for these 10 sources, which are also indicated by magenta filled circles** (Figure 9), following Ikeda et al. (2008). Six of 10 sources **(#1-2, #6-8, and #10)** are in the reddening zone of the classical T Tauri

star (CTTS) locus in Figure 8, but 4 of them **(#6-8, and #10)** are in the galaxy region above the reddening line (dashed-line) from the M0 giant star in Figure 9. These 4 sources are considered galaxy candidates, not YSO ones. Only #1 and #2 remain to be YSO candidates. #1 was defined as a Class II source (Koenig et al. 2008) and was reported to have Hα emission line (Ogura et al. 2002; Ikeda et al. 2008). Four excess sources **(#3-5, and #9)** are below the T Tauri locus (blue solid line) in Figure 8. Sources #3 and #5 lie near the M7 star position in Figure 9 and could be objects with lower temperatures. Source #3 was defined as a Class II source (Koenig et al. 2008). The other 2 sources **(#4 and #9)** are possible candidates for distant Herbig Ae/Be stars or classical Be stars, but may be background ones because of their faintness. Thus we regard #1, #2, and #3 sources as YSO candidates around SFO 12 **(Table 3) and #2 source is a newly identified YSO candidate in this work.**

We further searched for YSO candidates by using online data. Koenig et al. (2008) searched for YSO candidates and classified them into 3 types, Class I, Class II, and Class III, by using the Spitzer Space Telescope data. Hα emission stars around SFO 12 were first searched by Ogura et al. (2002), but the equivalent widths of Hα emission were not scaled from pixels to angstroms in their Table 5. Ikeda et al. (2008) rescaled the equivalent widths and published them online. We show these Class I to III sources, and Hα emission stars as well as our YSO candidates identified above as YSO candidates in Figure 2.

As shown in Figure 2, almost all of these YSO candidates are distributed toward the exciting star side of SFO 12. The Class II candidates (green circles) are mostly located just near the cloud edge facing the exciting star, while the Class III ones (cyan circles) are mostly located away from the cloud (upper right half of Figure 2). Two Class I candidates (red circles), **which correspond to the cluster members S3 and S6,** are located at the inner part of the SFO 12 head, and one is located at the tip of SFO 12W, which is a very small, **isolate** bright-rimmed cloud **separated** $\sim$40$''$

west of SFO 12, **probably just behind SFO 12 (see the appearance of SFO 12W in Figures 1 and 2). Here we postpone discussion of this small cloud, apparently separated from SFO12, to another paper combining Subaru and radio interferometer data (Fukuda et al. in preparation).**

3.4. *Photometric properties of the cluster members*

We examine the distribution of the cluster members on the $J-H$ versus $H-K_{\rm s}$ and $H-K$ versus $K-L'$ diagrams (Figure 10) by using the photometry results of 1.26 μm (J), 1.67 μm (H), 2.11 μm ($K_{\rm s}$) from the UH88 data and 3.77 μm (L') from the Subaru data (see Tables 1 and 2). Because S1 and S2 have envelopes, we performed photometry with an aperture larger than that of the others (column 7 of Table 1). Although S2 and S3 are binary systems, photometry was not performed separately for each star with the UH88 images. Because of the differences between the photometry apertures for the UH88 and Subaru images, the measured magnitudes are slightly different. The objects with their envelopes, S1, S2 and S4, tend to have smaller magnitudes in the photometry of the UH88 data than in that of the Subaru data. Due to the saturation of S3a in the Subaru H/K images, we did not perform the photometry of S3a at H and K.

S3 and S4 have large near-IR excess, while S1, S2, S5, and S6 show no near-IR excess on the $J-H$ versus $H-K_{\rm s}$ diagram (Figure 10a) and it is difficult to discriminate them from reddened field stars. However, S5 and S6 are located redward of the reddening zone of the CTTS locus on the $H-K$ versus $K-L'$ diagram (Figure 10b), and S6 was classified as Class I by Koenig et al. (2008). To examine this inconsistency in detail, we made a SED diagram of the 6 cluster members (Figure 11) using the Spitzer photometry data of 3.6 μm, 4.5 μm, and 5.8 μm. **Although the data points are not enough to formally calculate the infrared spectral index α defined at wavelengths of $2-10\mu$m (Lada 1987), we tried to roughly estimate the α indexes of S1 to S6 for YSO**

classification only with the data available (Figure 11; Tables 1 and 2).

The specific fluxes of S3 and S4 clearly increase longward of ~ 2 μm wavelength, and it is likely that they are Class I sources **with estimated α of ~ 0.31 for S3 in the wavelength range of $\sim 2-6$ μm and ~ 0.43 for S4 in the narrower range of $\sim 2-4$ μm (Greene et al. 1994). The 12 μm flux ($\sim$330 mJy) of WISE is also available for S3 (see the note of Table 2), but its resolution of 6.″5 (Wright et al. 2010) might cause contamination from S4 and S5. However it is most likely that most of the long wavelength emission comes from the brightest source S3, in which case the estimated α is valid. Although no flux data are available for S4 at a longer wavelength of > 4 μm, the protostellar-like shape of its envelope suggests a high probability of Class I.** On the other hand, **the specific fluxes** of S1 and S2 decrease longward of ~ 2 μm wavelengths and it is likely that they are Class II sources **with $\alpha < -0.6$ for S1 and < -0.2 for S2, which are deduced from their L' upper limits. With their circumstellar envelopes and embedded locations within the cloud, they would be** younger than general Class II sources with ages of ~ 1 Myr **if they are really Class II sources without significant flux excess/rise at wavelength of > 4 μm**. S5 and S6 show rather flat energy distribution longward of ~ 2 μm wavelength and seem to be **flat SED sources with estimated α of ~ -0.06 for S5 in the narrow wavelength range of $\sim 2-4$ μm and ~ 0.03 for S6 in the wavelength range of $\sim 2-6$ μm (Greene et al. 1994; Dunham et al. 2014), although S6 was classified as Class I by Koenig et al. (2008).**

We show J versus $J-H$ and color-magnitude diagram with the isochrones of Siess et al. (2000), adopting 2.2 kpc as the distance to SFO 12 (Figure 12). Generally, it is difficult to estimate the ages of YSOs, so here we simply adopted a plausible range of ages, $\sim$0.3 to 1.0 Myr, for the cluster members to roughly estimate their masses. S1, S2, S5, and S6 appear to be low-mass stars with masses of ~ 1 $M_\odot$ or less. On the other hand, S3 appears to be an intermediate mass star with a mass

of $\sim$3 $M_\odot$ or higher, and this could be consistent with the luminosity of IRAS 02511 +6023, which was estimated by Morgan et al. (2008). Judging from this diagram, S4 would be a very low-mass star, but the H-band shape of S4 suggests that its flux comes from the corn-shaped reflection nebula (Figure 6), thus S4 fluxes of J and H would be underestimates, and could be intrinsically larger. Taking into account the L'-band specific flux of S4 (Figure 11), it might have a mass similar or larger to those of S5 and S6. **We can estimate an Av (column 8 of Table 1) from the source positions in the color-magnitude diagram, which are similar to those estimated from the color-color diagram (Figure 10a) for S1, S2, S5 and S6. For S4 we can only estimate a lower limit due to underestimated J and H band fluxes, because these fluxes might be those of reflection light from less dense areas in the S4 envelope (e.g., Section 3.2).**

We also try to make rough calculations of bolometric temperatures, $T_{\rm bol}$, for the cluster members with their limited flux data and Av estimated in the previous paragraph, following Chen et al. (1995). They derived $T_{\rm bol}$ only for YSOs that have been detected at six or more wavelengths in the rage of 0.3-1200 μm. Here, it is hard to accurately calculate $T_{\rm bol}$ due to the limited flux data, but we expect this trial help us get some hints or support for the YSO classification. $T_{\rm bol}$ can be calculated to be $\sim$ 1400 K for S3 and $\sim$ 1200 K for S4, only with the data points listed in Table 1 or 2. Although these values are those of Class II sources (Chen et al. 1995; Dunham et al. 2014), they may be the upper limits due to lack of longer wavelength data. In fact, $T_{\rm bol}$ of S3 can be derived to be $\sim$180 K, which is that of Class I sources, by adopting the WISE 12 μm and 22 μm fluxes (footnote of Table 2) and the 60 μm and 100 μm fluxes in the IRAS HiRes images (Table 1 of Morgan et al. 2008) as the fluxes that come entirely from S3. If S4 has SED distribution analogous to that of S3 at wavelength of $\gtrsim$ 4 μm, $T_{\rm bol}$ of S4 would also be much lower than $\sim$ 1200 K. In the same way only with the available data in Table 1 or

2, $T_{\rm bol}$ can be calculated to be ∼2100 K for S1 and S2, ∼2000 K for S5, and ∼1800 K for S6. However, the actual $T_{\rm bol}$ of S5 and S6 might be lower than these calculated values, considering their possible flat SED. If the fluxes of S1 and S2 simply decrease longward of $\gtrsim$ 2 μm, the calculated values of ∼2100 K would not be so inappropriate.

3.5. *H_2 column density map*

Figure 13a shows the H_2 column density map derived from the *Herschel* archival data mentioned in Section 2.4.2. For comparison, the Hα image is shown in Figure 13b. The column density is relatively higher at the boundary region directly irradiated by UV from the exciting star than on the opposite side. Figure 13a could identify a head-tail structure, which comprises a dense head part around S3 and two wings that extended from the head part toward the opposite side of the main exciting star. The length of this structure is ∼300″ (∼3.2 pc at d = 2.2 kpc). These wing features cannot be identified in the 850 μm contour map of Morgan et al. (2008), while they are clearly seen in our column density map. A sign of these features can be seen in the column density map in Deharveng et al. (2012). SFO 12 was classified as type B from the optical image by Sugitani et al. (1991), but we reclassify it here as type C (cometary bright-rimmed cloud), because it shows a head-tail structure with two wings.

A high density peak of ∼1.2×10^{22} cm^{-2} is found in the immediate vicinity of S3. The dust temperature is derived to be ∼22-24 K toward the density peak. The mass of the dense head part around the density peak of ∼0.9′×1.1′ was calculated to be ∼20 $M_\odot$ and the entire mass from the head part up to the ends of two wings to be ∼50 $M_\odot$. The mass derived toward the dense head part is consistent with that of Morgan et al. (2008) if we consider a difference of the adopted distances.

In order to examine these wing-like structures in more detail, we present the CO (J = 3-2) data that enable us to probe their velocity structures in the next subsection (Section 3.6).

3.6. *CO (J = 3-2) Emission*

Channel maps of CO (J = 3-2) are shown in Figure 14a-e. The systematic velocity around SFO 12 seems ~ -38.10 km s^{-1} with the highest intensity. This velocity is consistent with the ^{13}CO (J = 1-0) velocities of cloud 1 of Niwa et al. (2009), -38.3 km s^{-1}, and of the cloud of IRAS 02511+6023 of -38 km s^{-1} (Table 1 of Carpenter et al. 2000). Figure 14a and Figure 14e give a hint that a molecular outflow is associated with S3 and/or the other cluster members. This outflow was first noticed by Sugitani & Ogura (1994). To make sure this outflow is associated with the cluster, we made a CO (J = 3-2) profile toward S3 (Figure 15) and contour maps of the blue- and red-shifted emission (Figure 16). It is clear that the molecular outflow is associated with the cluster and that the distribution of the cluster members appears to correlate with the outflow emission. But it is unclear which source is the main one driving this outflow because of insufficient resolution of the single dish beam. The blue-shifted and red-shifted emissions are significantly overlapped. If the outflow is driven by a single source, its axis would be close to the line of sight.

The emission corresponding to the two tails (wings), which has already been shown in the column density map in Figure 13, is seen in Figure 14a, b, and c. The most blue-shifted tail emissions can be recognized toward the dead ends of the tails at the opposite side of the head. As the velocity approaches the systematic velocity, the tail emission becomes stronger toward the head. The red-shifted emission is confined only near the head (Figure 14d). Thus these tails seem to have a velocity gradient, and we will discuss the velocity structure later.

4. DISCUSSION

4.1. *Star formation toward the head of SFO 12*

Several Class II sources (Koenig et al. 2008) including Hα emission stars (Ikeda et al. 2008) are distributed in the region just outside the cloud head on the side of the main exciting star (Figure 2).

On the other hand, little sign of star formation is seen toward the tails on the opposite side of the dense head part, implying the UV impact on star formation around SFO 12.

In Section 3.4 we derived the best possible YSO classifications from the flux data available to us, where we feel quite confident about our classifications for S3 and S6. The YSO class stages (class I, II, III) does not always correspond to a chronological order of YSOs, and there may be age overlap between the adjoining classes in real YSOs (e.g., Dunham et al. 2014). Nevertheless we can discuss the formation history of the cluster members under the clear assumption that the YSO class order *does* **correspond to their chronological order.**

Among the cluster members, S3 and S4 would be the youngest with **our classification of Class I. Actually,** S3 has the largest excess (Figures 10 and 11) and was classified as Class I **by Koenig et al. (2008).** S4 has the second largest excess and the cone-shaped reflection nebulosity (Figure 6). In addition, they are located closest to the highest density peak of the cloud head in Figure 16. S5 and S6 would be the second youngest with **our classification of flat-SED**. Although S5 and S6 show no near-IR excess at the wavelengths shorter than K-band, they show excess at the wavelength of L'-band or longer (Figure 11). Further, they are also located close to the highest density peak in Figure 16. **S1 and S2 would be the oldest among these members with our classification of Class II.** They, **with remarkable circumstellar envelopes (Figures 4 and 5),** are situated toward the slightly less dense edge of the cloud head, **while** the column density of their positions are still high, $\sim$6-8$\times10^{21}$ cm^{-2}. Thus, they are considered to have the ages younger than that of usual Class II sources. These considerations**, under our rough classification and above assumptions,** indicate that formation of S1 and S2 occurred in advance of S3 to S6.

Secondly, we consider the case that our classification and the above assumptions are not valid. Even if our supposed age difference of the cluster members is not the case,

they would have been formed after the formation of the several Class II sources just outside the cloud head, since they are still embedded in the cloud head. Thus, the existence of these several Class II sources as well as the elongated distribution of the cluster members (see Section 3.2) support the idea that star formation took place from the cloud tip to the cloud center due to the UV impact from the main exciting star.

The alignment direction is nearly the same as that of the incident uv radiation (PA∼118°, Section 3.2). However, the several Class II sources just outside the cloud head are slightly out of this alignment line of the cluster members. Two possible causes of this small misalignment can be considered. One is that the several Class II sources were formed in another, small cloud, which had been very close to the cloud head. The other possibility is that the UV incident direction changed due to the movement of the main exiting star **(BD +60 586 A). The recently reported proper motion of Gaia DR1 for BD +60 586 A (GAIA ID 464697869244818560; Gaia Collaboration 2016)** is (pmRA, pmDec) = (0.223 ± 0.450 mas/yr, 0.079 ± 0.460 mas/yr). If it has been moving for ∼1 Myr with this reported proper motion, the main exciting star is estimated to have moved a few arcminutes. Although the error of proper motion is relatively larger than the proper motion itself, the movement of the main exciting star might be small. **In this case the small misalignment can plausibly be due to motion of the main exciting star. We can therefore conclude that sequential star formation may have taken place, although we can't prove it. We also note from our observations that there *may* be an additional small cloud toward the tip of SFO 12, but the far-infrared/CO data currently available (e.g. Figures 13 and 14) are as yet inadequate to confirm this.**

4.2. *Global structure of SFO 12*

SFO 12 is located at the periphery of the H II region and it is certainly affected by strong UV from the main exciting star. In that case, the molecular gas might be accelerated and compressed by the ionizing reaction of molecular gas. In the center of the cloud head, part of the accelerated gas is expected to form stars due to the shock compression by RDI. The gas in the two side ears would be accelerated and blown away toward the opposite side of the head part, and become visible to us as two tails due to the limb brightening effect. We interpret the velocity structure from this point of view.

The optical depth of ^{12}CO is larger than those of ^{13}CO and C^{18}O, and ^{12}CO can sample only the gas of low density and/or of the cloud surface. The gas of high density should be toward the center of the cloud head, where the cluster formed. The resolution of the archival ^{13}CO and C^{18}O single-dish data are insufficient to resolve the high density part because of the relatively large beam size. Therefore it is hard to examine the high density part of the cloud head in detail with the archival single-dish data. However, the elongated distribution of the cluster members suggests that the high density core to form stars was elongated.

The gas of the tails shows the blue-shifted velocity with respect to the cloud head as shown in Figure 14a and Figure 14b. This suggests that the gas of tails is blown off from the cloud head toward the near side (see Figure 17). This view is supported by the optical appearance that the far side surface of the cloud head is more strongly irradiated than the that of the near side as shown in Figure 13b. The red-shifted gas toward the head (Figure 14d) may correspond to some parts of the gas flowing along the surface of the cloud head.

4.3. *Comparison of SFO 12 with the RDI model*

Theoretical investigation on the formation of BRCs under RDI mechanism (Miao et al. 2009; Haworth et al. 2012; Kinnear et al. 2015) revealed that the morphology of a BRC

is dependent on both the ionising radiation field and the initial density of the molecular cloud. When an ionising source is fixed, the morphology of a BRC after RDI is decided by the initial density of the molecular cloud (Miao et al. 2009; Kinnear et al. 2015). The curvature of the surface of the front hemisphere of a BRC increases with the decrease in initial density of a molecular cloud of given initial mass. This is because the initial density of a cloud of a given mass decides the level of its initial gravitational binding, and the latter determines how the gas in the two sides of the flattened front hemisphere move after they pass the front hemisphere. A qualitative analysis on the direction of the total velocity of a point mass at the front surface of a cloud can clearly reveal the picture **(see Figure 18 from Figure 5 of Miao et al. 2009).**

After a short time of the RDI action, the front half of the cloud deviates from the original shape of a hemisphere, i.e., the front surface gets flattened (as shown in Figure 7 of Bertoldi 1989). The negative normal vector at each point of the front surface does not point to the gravitational center G, instead its directional line crosses the central line at a point C' which is behind the G point. The velocity of a point mass at any point of the front surface is composed of two components. The first one is the shock component $V_{\rm C} \propto 1/\sqrt{n}$ (Lefloch & Lazareff 1994) caused by RDI action and aligned with the negative normal vector of that surface point, and the other one is the gravitational component $V_{\rm G} \propto \sqrt[3]{n^2}$, resulting from the gravitational acceleration at that surface point and always pointing to the gravitational center G. The total velocity $V_{\rm T}$ is the vector sum of $V_{\rm G}$ and $V_{\rm C}$, whose directional line crosses the central axis at a point **C'** between G and **C**. The further away this crossing point is from the original gravitational center G, the higher the probability the shape of the BRC is to be type C.

We assume that there are two initially spherical clouds of same initial uniform mass, and cloud 1 is of lower initial density than cloud 2. Cloud 1 would have a higher probability to become type C BRC than cloud 2. This is because at any point of the front surface, a point mass at the front surface of

cloud 1 has a lower $V_{\rm G}$ and a higher $V_{\rm C}$ than that of cloud 2. The directional line of the total velocity $V_{\rm T}$ of the point mass in cloud 1 crosses the central axis of the cloud at point C' which is further away behind the initial G point than that in cloud 2. The mass flow toward the farther point C' in cloud 1 makes the formation of a type C BRC more likely than in cloud 2. It takes a longer time to form a type C BRC as well. The head structure in a type C BRC always has an elongated shape along the ionizing radiation direction. The latest work with higher resolutions by Kinnear et al. (2015) on the morphological evolution of spherical/non-spherical molecular clouds under the effect of RDI further supports the above conclusion, and found the elongated core sometimes could fragment into a few separated cores due to gravitational instability of elongated condensed linear structures developed during the RDI process.

Our analysis of archival data proves that SFO 12 has a long tail structure and the dense head facing the main exciting star, i.e., it is a type C BRC. Our near-IR observations suggest the existence of the elongated core to form cluster members within the head. According to the model prediction, the formation of long tails shows that the initial density of the cloud is not high, and that it takes a relatively long time to create the elongated core to form cluster members. We roughly estimated the time scale of the long tail formation. Adopting a tail length of 3.2 pc and assuming a flow velocity of the tails of a few km s^{-1}, it may be plausible to derive its time scale from the blue-shifted velocity of the channel maps (Figure 14), which is shown to be $\sim$1 Myr. The ages of the cluster members could be even less than $\sim$1 Myr, because they are still embedded in the cloud head. Therefore we conclude cluster formation might be possible by RDI in the type C BRC SFO 12.

5. SUMMARY

We conducted optical and near-IR (Hα, [SII], i', J, H, K') observations with UH88, and high-resolution near-IR observations (H, K, L') with the AO system of Subaru to examine star formation

in SFO 12. We also used the archival data of far-infrared and CO (J = 3-2) to examine the cloud structure. Our work is summarized as follows.

1. We found a small YSO cluster of six members (S1-S6) embedded in the head of SFO 12 facing its exciting star, and that they are nearly aligned along the UV incident line from the exciting star.

2. We revealed that three of the cluster members (S1, S2, and S4) appear to have circumstellar envelopes, and that one of them (S2) shows an arm-like structure in its envelope. We also revealed that two of them (S2 and S3) are binary systems.

3. Our photometry and the Spitzer IRAC data suggest that formation of two members (S1 and S2) located at the tip side occurred in advance of other members (S3, S4, S5, and S6) located at more central part of the head, **under our adopted assumptions**.

4. Our near-IR data and previous studies imply that more YSOs are distributed in the region just outside the cloud head on the side of the main exciting star, but there is little sign of star formation toward the opposite side of the head. Star formation might have been sequentially occurring from the exciting star side to the central part in the cloud head, i.e., a sequential star formation on small scale.

5. SFO 12 has a clear cometary shape (type C), i.e., a head-tail structure extended from the cloud head toward the opposite side of the exciting star in the far-infrared and CO (J = 3-2) although SFO 12 has a shape of type B in the optical.

6. The alignment line of the cluster members and the head-tail structure are nearly the same as the UV incident line from the main exciting star. This suggests that SFO 12 is certainly affected by the strong UV from the main exciting star, which has induced star formation in SFO 12.

7. We discussed the formation of this cometary shape and star formation there by comparing with the RDI model.

We are grateful to the staff of UH88 for supporting our WFGS2 and QUIRC observations. We also appreciate the great support of Subaru Telescope. The use of UH88 for the observations was supported by the National Astronomical Observatory of Japan. R. I. thanks the Daiko Foundation for financial support of our resarch. This work was partly supported by Grants-in-Aid for Scientific Research (17039011, 19540242, and 20403003) from the Ministry of Education, Culture, Sports, Science, and Technology of Japan.

REFERENCES

Aniano, G., Draine, B. T., Gordon, K. D., et al., 2011, PASP, 123, 1218
Bertoldi, F., 1989, ApJ, 346, 735
Bessell, M. S., & Brett, J. M., 1988, PASP, 100, 1134
Bessell, M. S., AJ, 101, 662
Bisbas, T. G., Wunch, R., Whitworth, A. P., Hubber, D. A., et al., 2011, ApJ, 736, 142
Buckle, J. A., Hills, R. E., Smith H., et al., 2009, MNRAS, 399,1026
Carpenter, J. M., Heyer, M. H., & Snell, R. L., 2000, ApJS, 130, 381
Chauhan N., Pandey A. K., Ogura K., et al., 2011, MNRAS, 415, 1202
Chen, H., Myers, P. C., Ladd, E. F., & Wood, D. O. S., 1995, ApJ, 445, 377
Choudhury, R., Mookerjea, B., & Bhatt, H. C., 2010, ApJ, 717, 1067
Cox, A. N. 2000, Allen's Astrophysical Quantities (4th ed.; New York: Springer)
Deharveng, L., Zavagno, A., Anderson, L. D., et al., 2012, A&A, 546, A74
Dunham, M. M., Stutz, A. M., Allen, L. E., et al., 2014, in Protostars and Planets VI, ed. H. Beuther et al. (Tucson, AZ: Univ. Arizona Press)
Fazio, G. G., Hora, J. L., Allen, L. E., et al., 2004, ApJS, 154, 13
Fukuda, N., Miao, J., Sugitani, K., et al., 2013, AJ, 773, 132
Gaia Collaboration, 2016, A&A, 595, A1
Georgelin, Y. M., & Georgelin, Y.P., 1976, A&A, 49, 57
Greene, T. P., Wilking, B. A., Andre, P., 1994, AJ, 434, 614
Griffin, M. J., Abergel, A., Abreu, A., et al., 2010, A&A, 518, L3
Gritschneder, M., Naab, T., Burkert, A., Walch, S., Heitsch, F., & Wetzstein, M., 2009, MNRAS, 393, 21
Hawarden, T. G., Leggett, S. K., Letawsky, M.B., et al., 2001, MNRAS, 563, 574
Haworth, T. J., Harries, T. J., & Acreman D. M., 2012 MNRAS, 426, 203
Hodapp, K. W., Hora, J.L., Hall, D. N. B., et al., 1996, NewA, 1, 177
Ikeda, H., Sugitani, K., Watanabe, M., et al., 2008, AJ, 135, 2323
Ishida, K., 1970, PASP, 22, 277
Johnson H. L., Hoag A. A., Iriarte B., et al., 1961, Lowell Obser. Bull., 5, 133
Jordi, K., Grebel, E.K., & Ammon, K., 2006, A&A, 406, 339
Karr, J.L., & Martin, P.G., 2003, ApJ, 595, 900
Kessel-Deynet, O., & Burkert, A., 2003, MNRAS, 338, 545
Kinnear, T. M., Miao, J., White, G. J., & Goodwin, S., 2014, MNRAS, 444, 1221
Kinnear, T. M., Miao, J., White, G. J., Sugitani, K., & Goodwin, S., 2015, MNRAS, 450, 1017
Koenig, X. P., Allen, L. E., Gutermuth, R. A., et al., 2008, AJ, 688, 1142
Konyves, V., Andre, Ph., Men'shchikov, A., et al., 2010, A&A518, L106
Kusune, T., Sugitani, K., Miao, J., 2015, AJ, 798, 60
Lada, C. J., 1987, In Star Forming Regions (M. Peimbert and J. Jugaku, eds.), pp. 1-17. IAU Symp. 115, Cambridge Univ., Cambridge.
Lefloch, B., & Lazareff, B., 1994, A&A, 289, 559
Lim, B., Sung, H., Kim, J.S., et al., 2014, MNRAS, 1451, 65
Mastumoto, T., Onishi, T., Tokuda, K., et al., 2015, MNRAS, 449, 123
Matuyanagi, I., Itoh, Y., Sugitani, K., et al. 2006, PASJ, 58, L29
Meyer, M.R., Calvet, N., & Hillenbrand, L.A., 1997, AJ, 114, 288
Miao, J., White, G.J., Thompson, M.A., & Nelson, R.P., 2009, ApJ, 692, 382
Miao, J., Sugitani, K., White, G.J., & Nelson, R.P., 2010, ApJ, 717, 658
Morgan, L. K., Thompson, M. A., Urquhart, J. S., et al., 2004, A&A, 426, 535
Morgan, L. K., Thompson, M. A., Urquhart, J. S., et al., 2008, A&A, 477, 557
Morgan, L. K., Urquhart, J. S., & Thompson, M. A., 2009, MNRAS, 400, 1726
Morgan, L. K., Figura, C. C., Urquhart, J. S., & Thompson, M. A., 2010, MNRAS, 408, 157
Murakawa, K., Suto, H., Tamura, M., et al., 2004, PASJ, 56, 509
Nakano, M., Sugitani, K., Watanabe, M., et al., 2012, AJ, 143, 61
Niwa, T., Tachihara, K., Itoh, Y., et al., 2009, A&A, 500, 1119
Ogura, K., Sugitani, K., & Pickles, A. 2002, AJ, 123, 2597 (OSP)
Panwar, N., Chen, W. P., Pandey, A. K., et al., 2014, MNRAS, 443, 1614
Poglitsch, A., Waelkens, C., Geis, N., et al., 2010, A&A, 518, L2
Rieke, G.H. & Lebofsky, M.J. 1985, ApJ, 288, 618
Sandford M.T., Whitaker, R.W., Klein, R.I., 1982, ApJ, 260, 183
Sharpless S., 1955, AJ, 60, 178
Siess, L., Dufour, E., & Forestini, M., 2000, A&A, 358, 593
Skrutskie, M. F., Cutri, R. M., Weinberg, M. D., et al., 2006, AJ, 131, 163
Smith, J. A., et al., 2002, AJ, 123, 2121
Sota, A., Maiz Apellaniz, J., Walborn, N.R., et al., 2011, ApJS, 193, 24
Sugitani, K., Fukui, Y., Ogura, K., 1991, ApJS, 77, 59
Sugitani, K., & Ogura, K., 1994, ApJS, 92, 163
Sugitani, K., Tamura, M., & Ogura, K., 1995, ApJL, 455, L39
Takami, H., Takato, N., Otsubo, M., et al., 1998, SPIE, 3353, 500
Takami, H., Takato, N., Hayano, Y., et al., PASJ, 56, 225
Tamura, M., Suto, H., Itoh Y., et al., 2000, SPIE, 4008, 1153
Uehara, M., Nagashima, C., Sugitani, K., et al., 2004, SPIE, 5492, 661
Urquhart, J. S., Morgan, L. K., & Thompson, M. A., 2009, A&A, 497, 789

Whitney, B. A., Wood, K., Bjorkman, J. E., et al., 2003, ApJ, 598, 1079

Wright, E. L., et al. 2010, AJ, 140, 1868

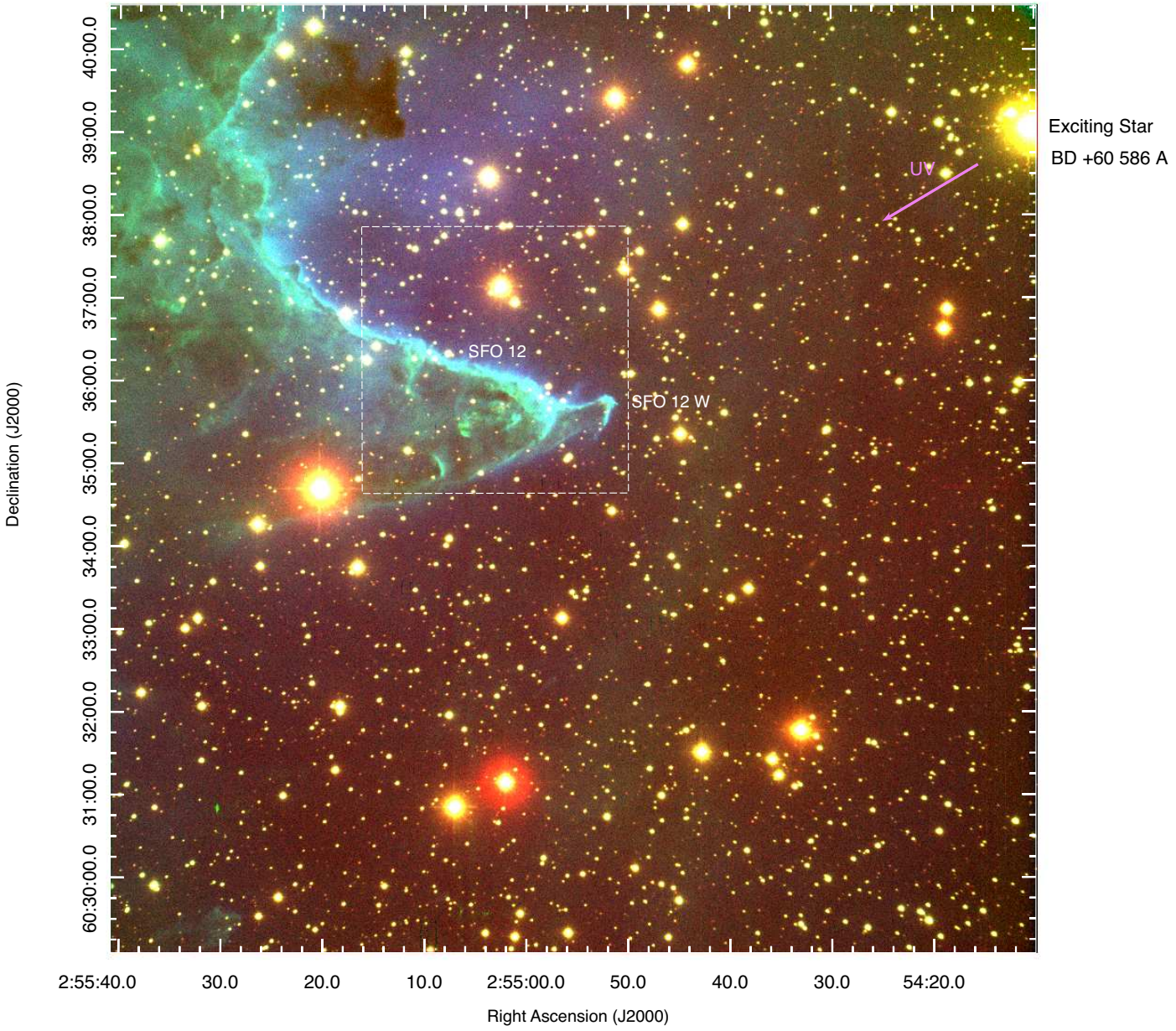

Figure 1. Three-color composite image of SFO 12 (blue, Hα; green, SII; red, i'). A dashed square box indicates the region of UH88 infrared observation. The main exciting star of the bright rim of SFO 12 (BD +60 586 A) is located at the upper right corner.

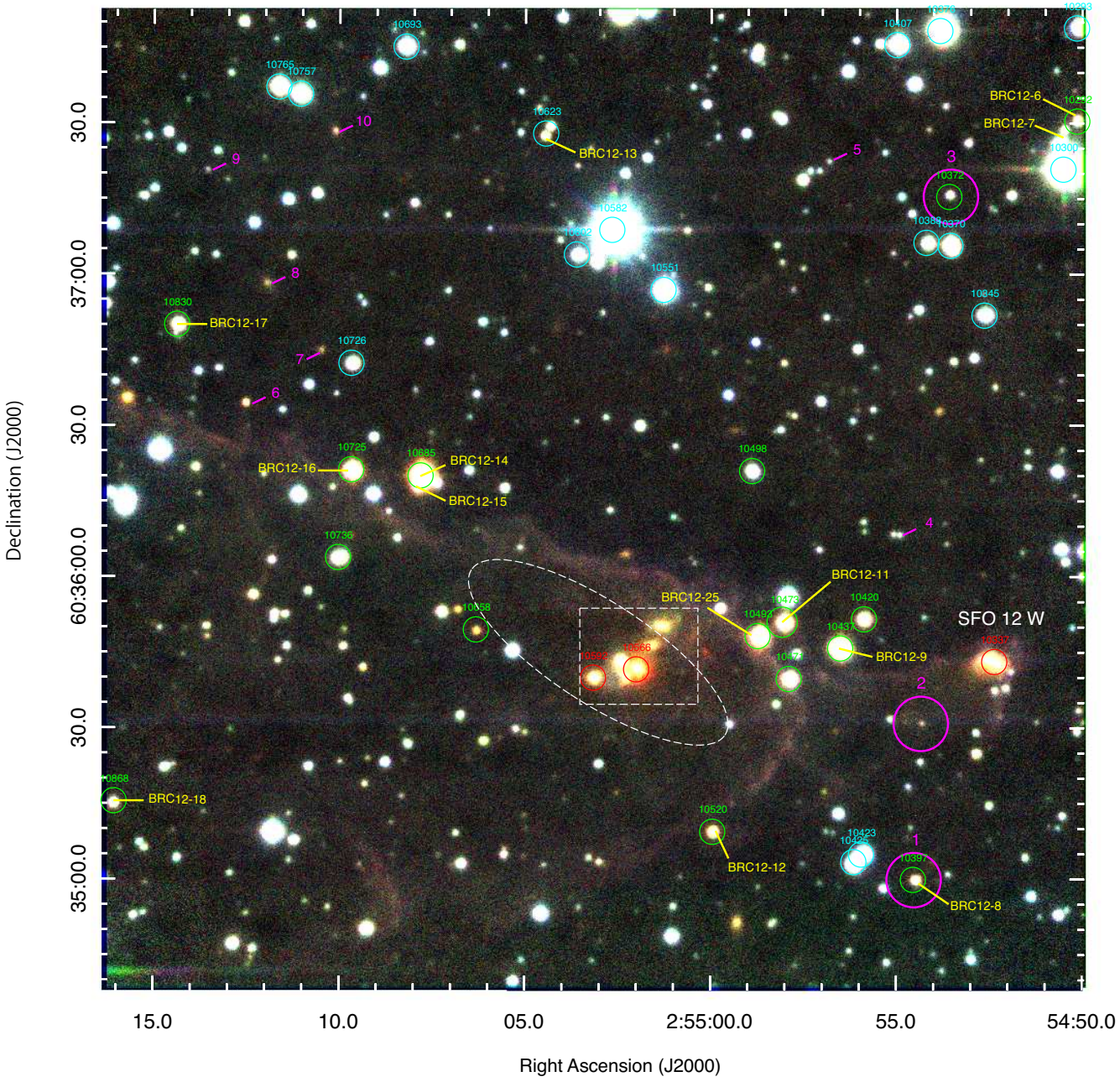

Figure 2. Three-color composite image toward SFO 12 (blue, J; green, H; red, K'). A dashed-line box indicates the region of the high-resolution infrared observation with Subaru. The position of IRAS 02511+6023 is shown with an error ellipse of position. Class I, Class II, and Class III sources (Koenig et al. 2008) are shown by red, green, and cyan circles, respectively, with ID numbers. Hα emission stars (Ikeda et al. 2008) are marked by yellow characters. Ten near-IR excess sources **described in Section 3.3 and in Figures 8 and 9 are marked by magenta-colored numbers (1-10). Among these numbered sources, #1-3 sources marked with magenta circles are selected as YSO candidates (see Section 3.3).**

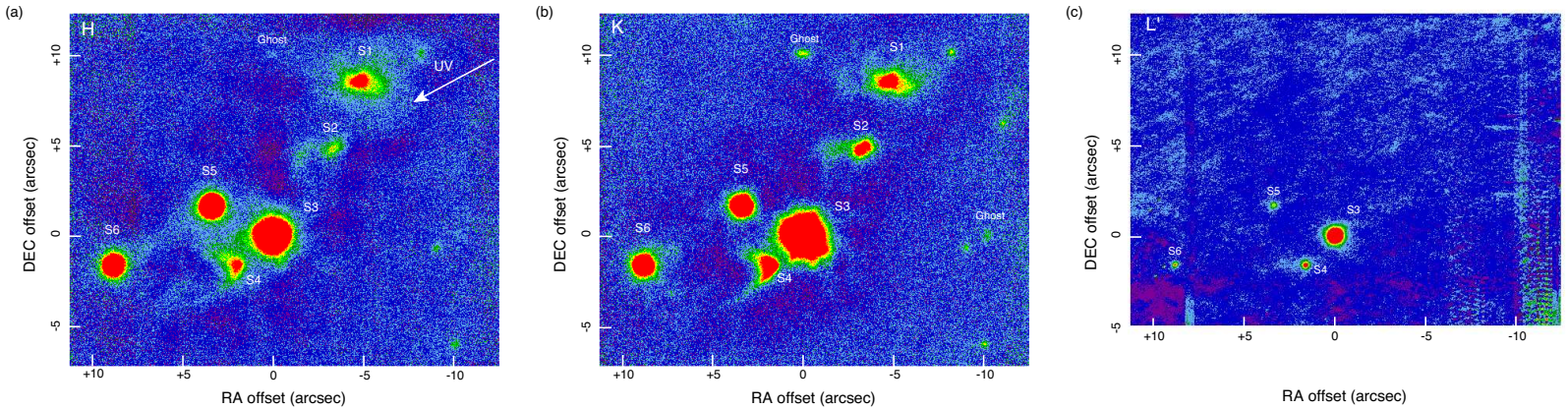

Figure 3. H, K, and L' images of SFO 12, obtained with Subaru/AO36 +CIAO. Six cluster members (S1-S6) are, YSO candidates, located toward the dense head part of the SFO 12 cloud. An arrow shows the UV incident direction from the main exciting star of SFO 12 on the left pannel.

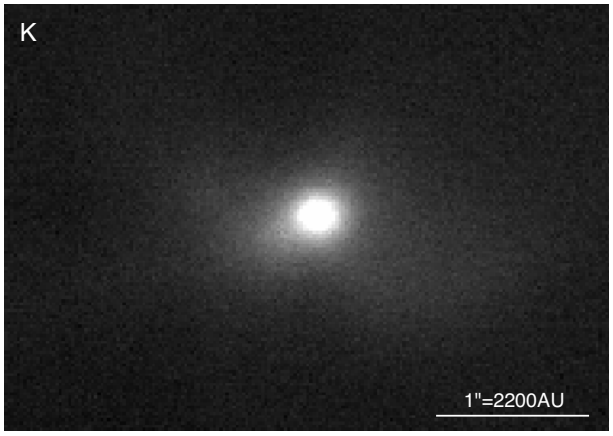

Figure 4. Close-up K image of S1, obtained with Subaru/AO36 +CIAO.

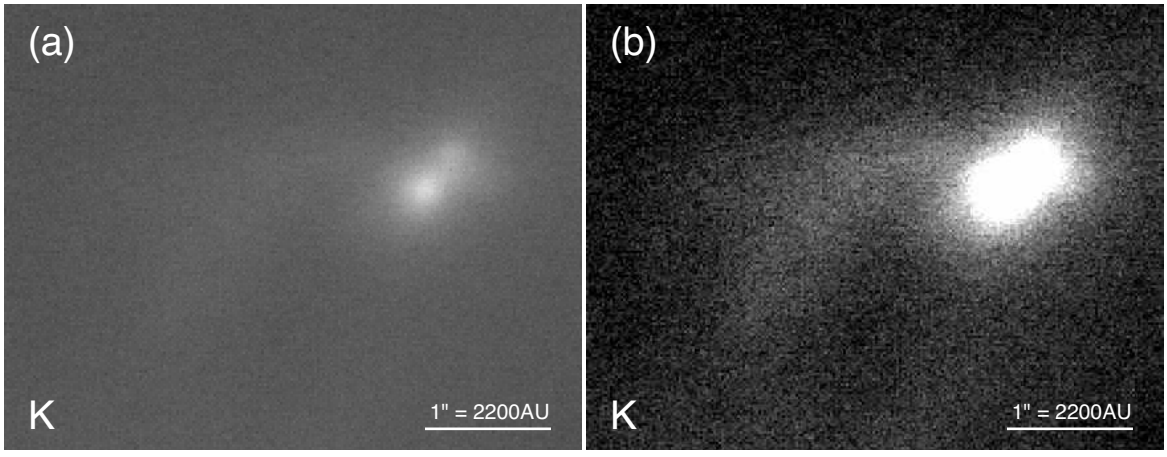

Figure 5. (a) Close-up K image of S2, obtained with Subaru/AO36 +CIAO, which shows that S2 is a binary system. (b) Display range changed K image, which shows an arm-like feature extending from S2.

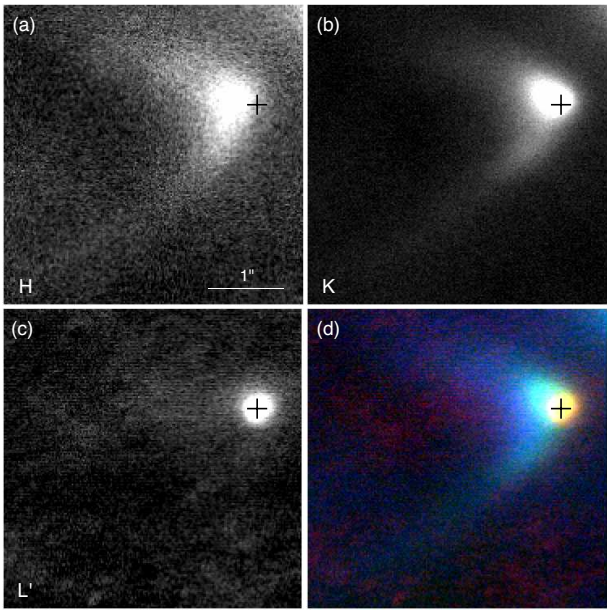

Figure 6. Close-up images of S4, obtained with Subaru/AO36 +CIAO. (a) H image. (b) K image. (c) L' image. (d) Three-color composite image (blue, H; green, K; red, L'). The cross shows the peak intensity position at L'.

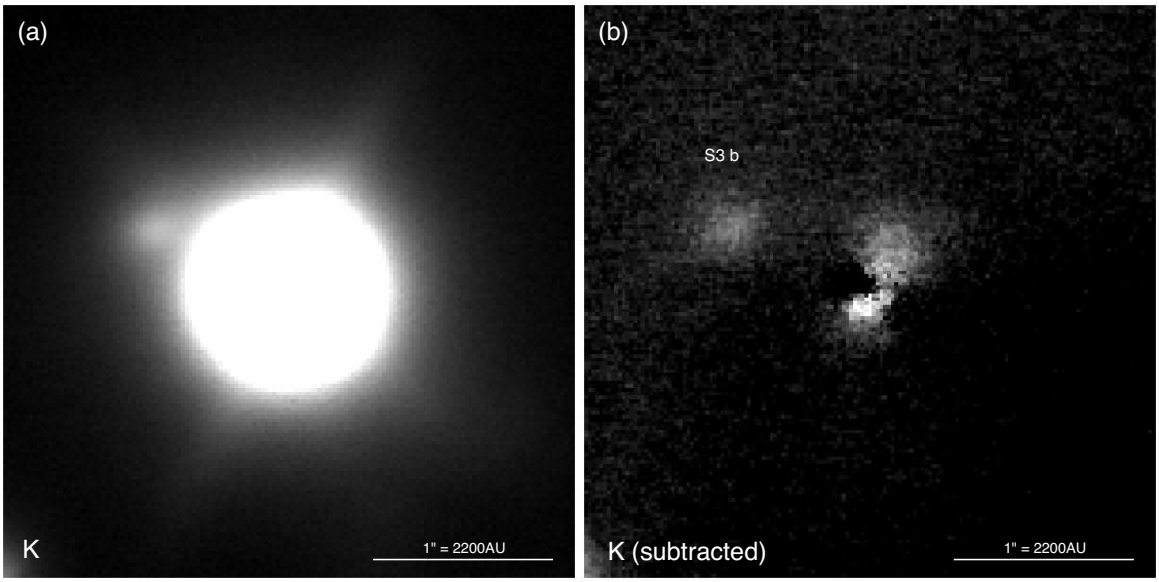

Figure 7. (a) Close-up K image of S3, obtained with Subaru/AO36 +CIAO. (b) A main stellar component subtracted image. We roughly scaled the intensity of S5 to that of S3, and subtracted the scaled image from the S3 image.

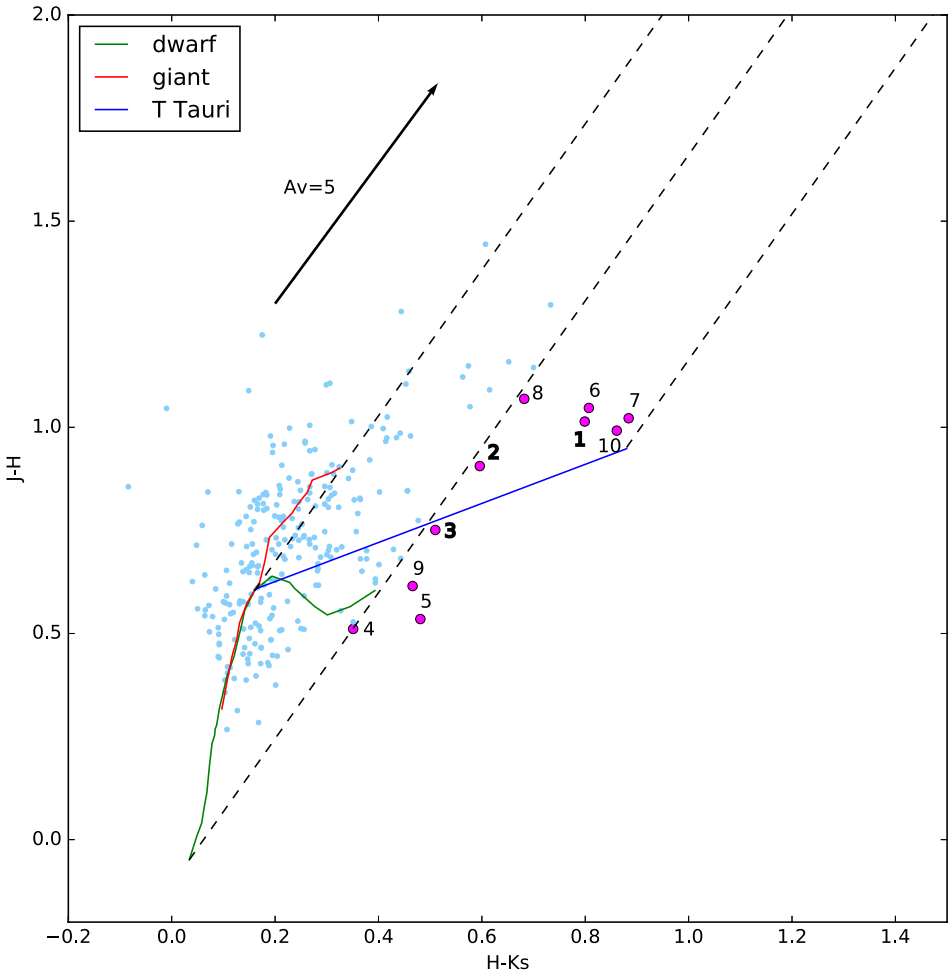

Figure 8. $J-H$ versus $H-K_s$ color-color diagram of near-IR sources detected by the UH88 observations. **Near-IR excess sources that are located redward of the reddening line from A0 star are plotted by magenta filled circles with ID numbers (#1-10) and are identical to those with magenta-colored numbers of Figure 2. Among them, 3 sources with bold ID numbers (#1-3) are selected as YSO candidates around SFO 12 (see Section 3.3).** The green and red solid curves show the dwarf and giant loci, respectively (Bessell 1988). The blue solid line shows the CTTS locus (Meyer et al. 1997). The dotted lines are parallel to the reddening vector. The colors for dwarfs, giants, and CTTS locus were transformed to those of the 2MASS system by using the equations of 2MASS web site (Section VI 4b, http://www.ipac.caltech.edu/2mass/releases/allsky/doc/sec6_4b.html). **The reddening vector was calculated from Rieke & Lebofsky (1985).**

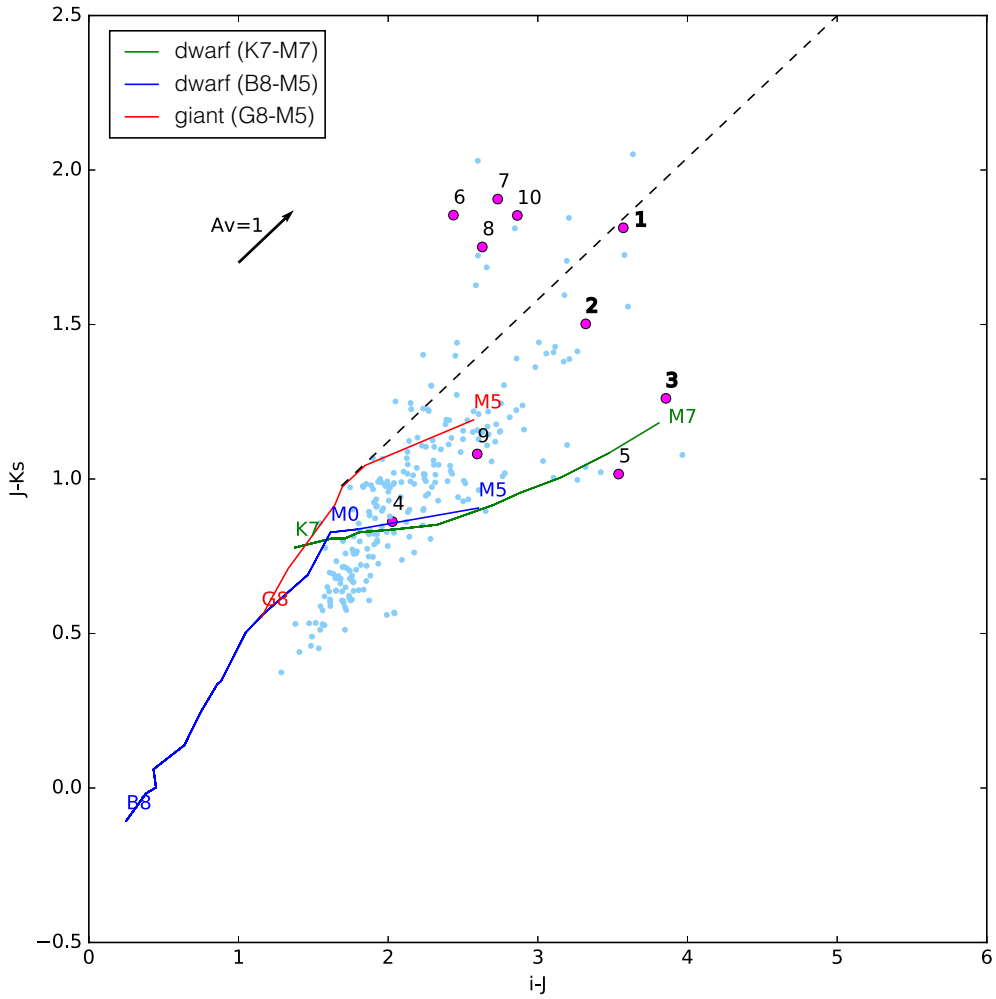

Figure 9. $J-K_s$ versus $i-J$ color-color diagram. **Ten near-IR excess sources of Figure 8 are plotted by magenta filled circles with ID numbers (#1-10) and are identical to those with magenta-colored numbers of Figure 2. Among them, 3 sources with bold ID numbers (#1-3) are selected as YSO candidates around SFO 12 (see Section 3.3).** The blue and green solid curves give the loci of dwarfs, and red solid curve give the locus of giants. The blue dwarf locus for B8-M5 and the red giant locus for G8-M5 are from Bessell (1988) and Table 15.7 of Cox (2000), respectively. The green dwarfs locus for K7-M7 is from Bessell (1991). The dashed line shows the reddening line from the M0 giant star. We used the transformation equation of Jordi et al. (2006) to obtain the i' magnitudes.

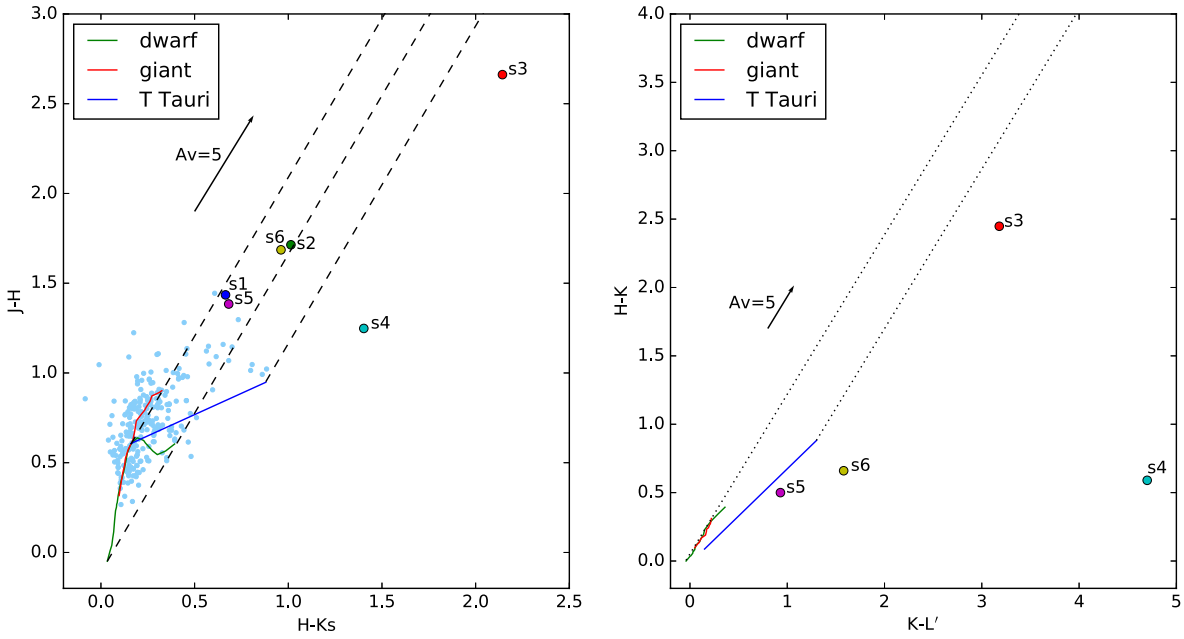

Figure 10. Color-color diagrams for the cluster members (S1-6), which are indicated by colored-circles. (a) $J-H$ versus $H-K_{\rm s}$ color-color diagram by using the photometry results of J, H, $K_{\rm s}$ from the UH88 data. The notation of this diagram is same as Figure 8. (b) $H-K$ versus $K-L'$ color-color diagram for the 4 cluster members (S3-6), by using the photometry results of H, K, and L' from the Subaru data, except for the H and K magnitudes of S3. The green and red solid curves give the loci of dwarfs and giants, respectively. The blue solid line give the locus of CTTS (Meyer et al. 1997). The $H-K$ data for dwarfs and giants were transformed to the MKO system by using the equations of 2MASS Web site (Section VI 4b, http://www.ipac.caltech.edu/2mass/releases/allsky/doc/sec6_4b.html). The H and K magnitudes of S3 in the MKO system were derived from the photometry results of UH88 also with the equation of 2MASS Web site. The $K-L$ data for dwarfs and giants are Bessell & Brett system. The arrow shows the reddening vector of Av=5. The reddening vector was calculated from Rieke & Lebofsky (1985).

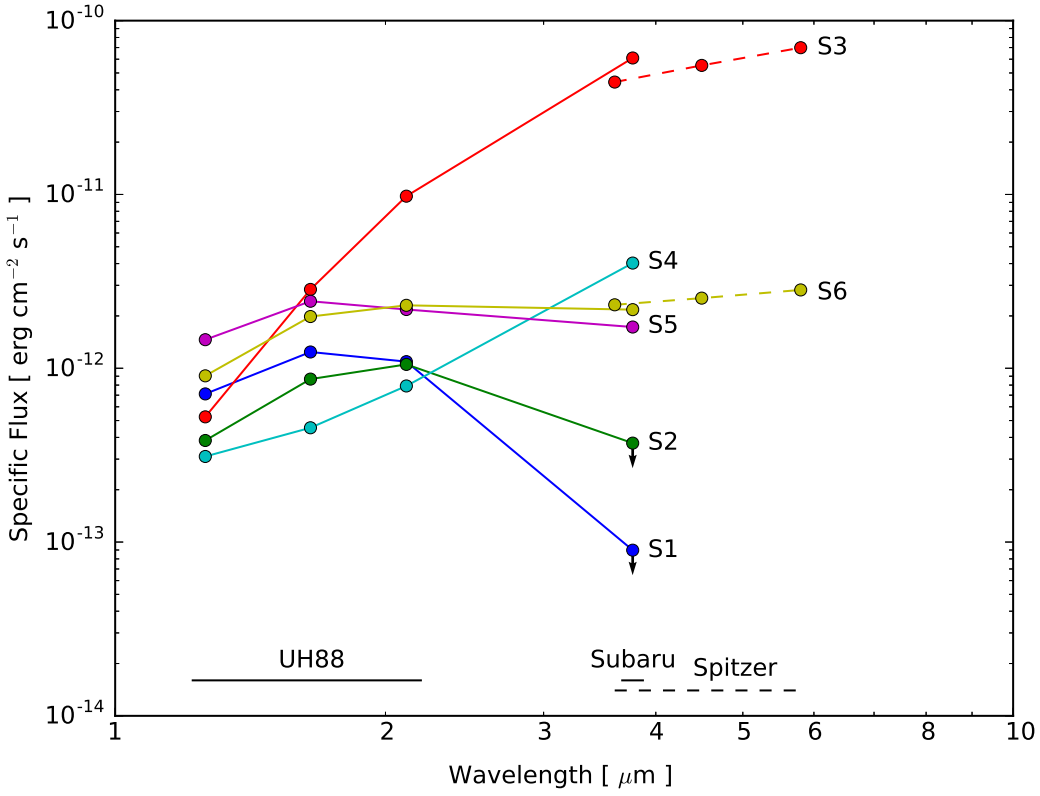

Figure 11. Spectral energy distribution of the six cluster members.

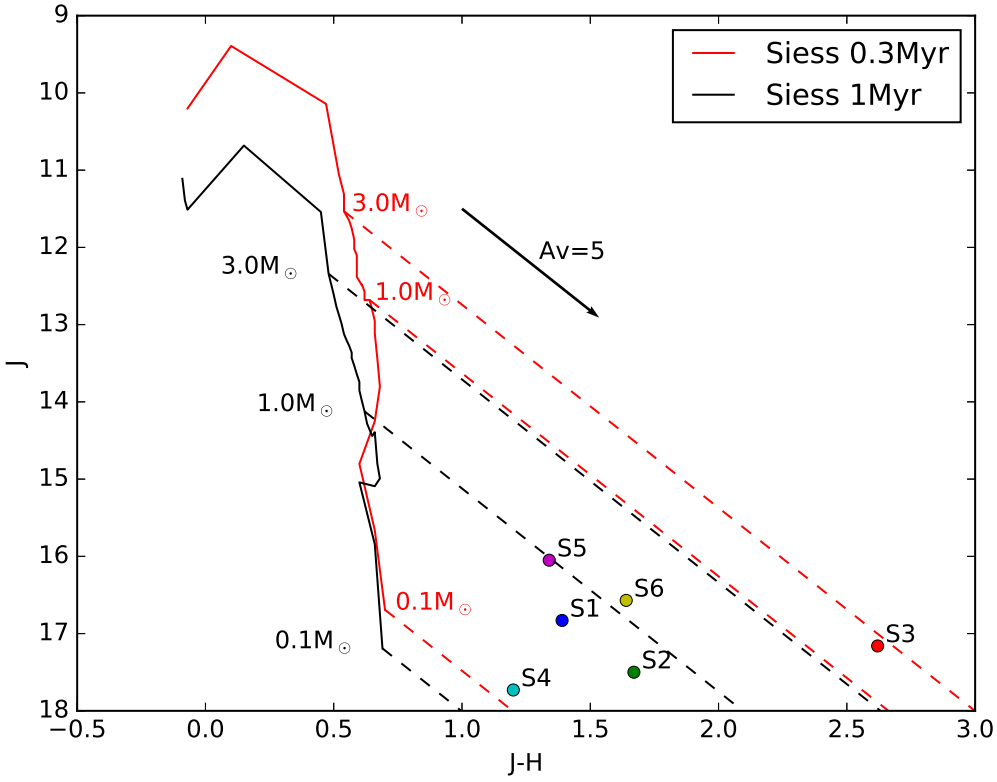

Figure 12. J versus $J-H$ color-magnitude diagram of the 6 cluster members (S1-S6). The black curve shows 1 Myr isochrones of Siess et al. (2000). The black dotted lines are parallel to the reddening vector from the positions of 3.0 $M_{\odot}$, 1.0 $M_{\odot}$, and 0.1 $M_{\odot}$. The isochrones and reddening vector for 0.3 Myr are also shown by a blue curve and blue dotted lines, respectively. S1, S2, S4, S5, and S6 appear to be low-mass stars, while S3 an intermediate one. The arrow shows the reddening vector of Av=5. The reddening vector was calculated from Rieke & Lebofsky (1985).

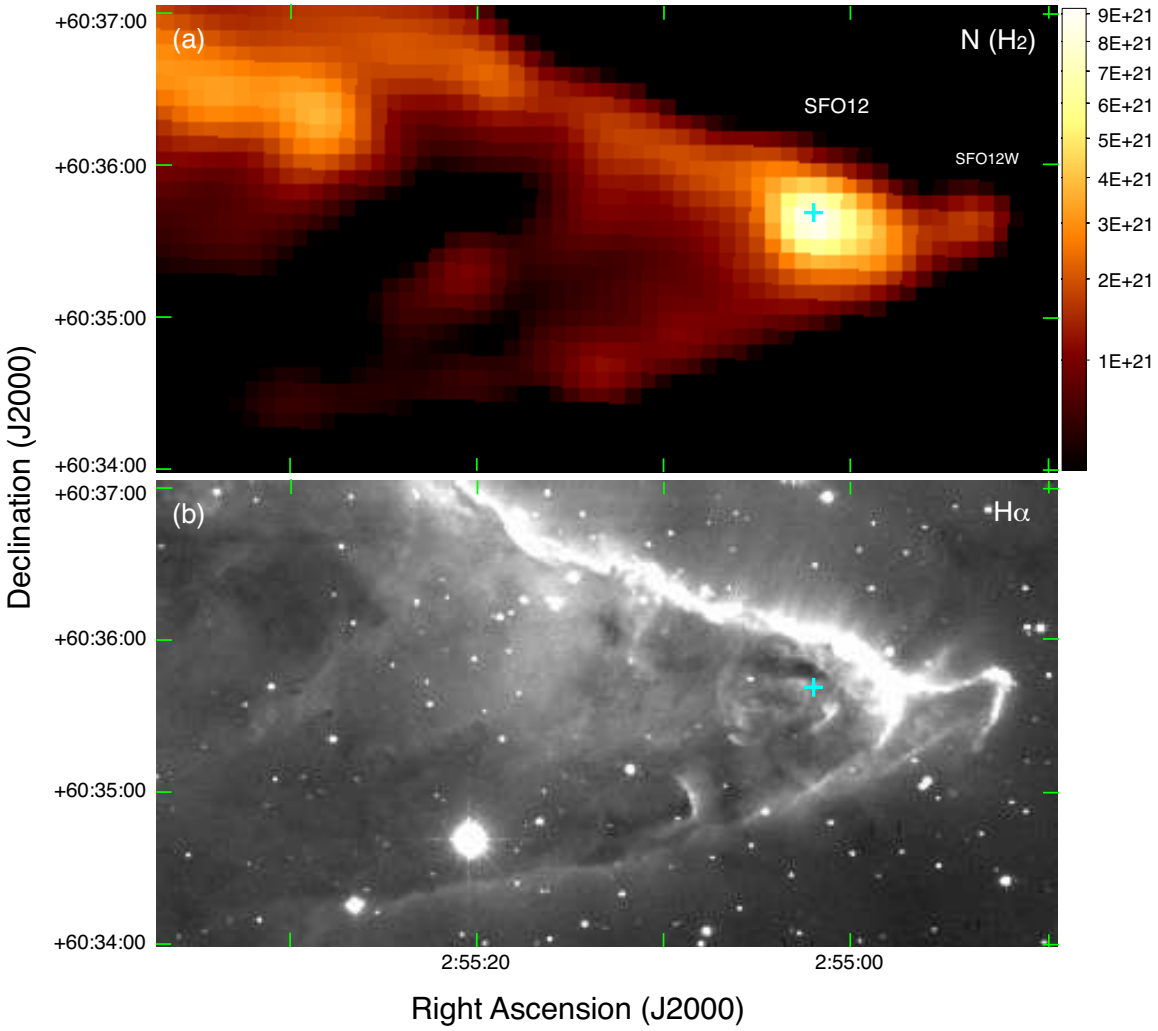

Figure 13. (a) H_2 column density map of SFO 12. The color bar gives a scale of the H_2 column density (cm^{-2}). (b) Hα image of SFO 12. A cross shows the position of S3.

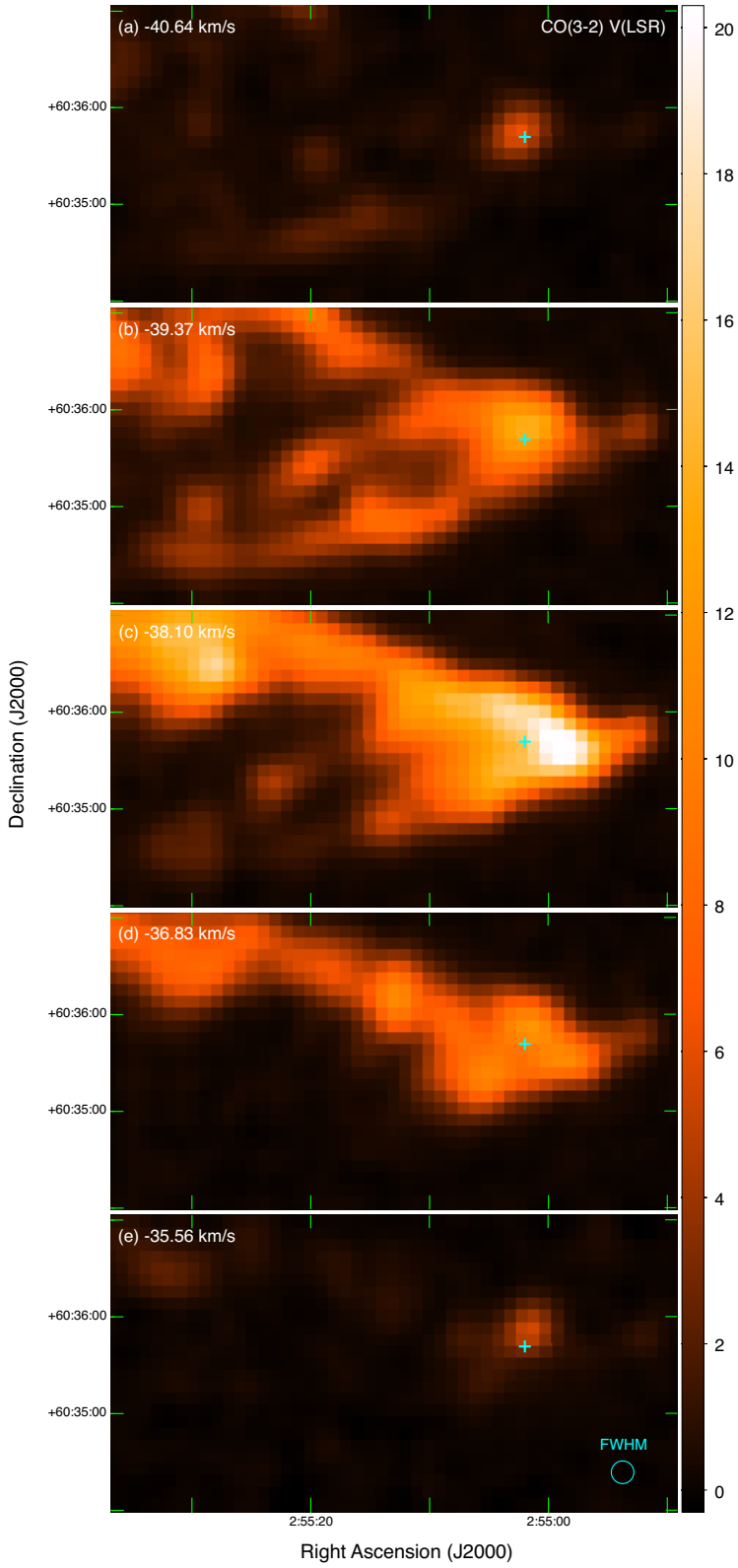

Figure 14. Channel maps of CO (J = 3-2). The color bar gives a scale of the integrate intensity of each channel in $T_{\rm A}^{*}$ (K km s^{-1}). The cross shows the position of S3. The beam size is shown in the lower right corner of the bottom panel.

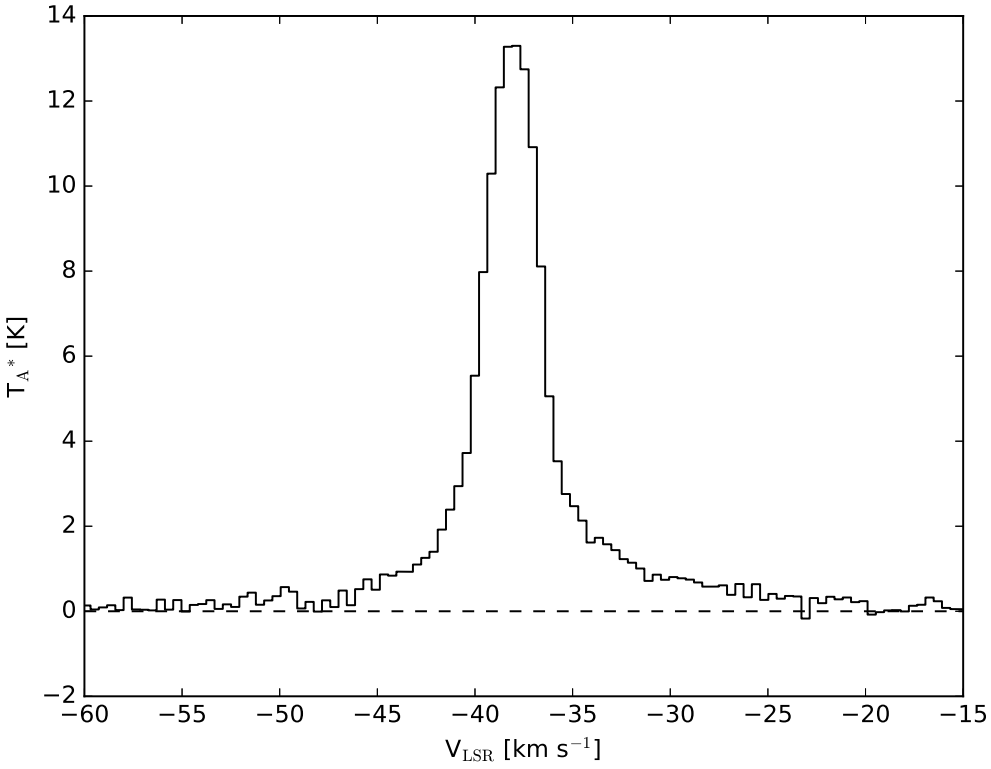

Figure 15. CO (J = 3-2) mean profile toward S3. The profile is regionally averaged within a circle with a radius of 14″.

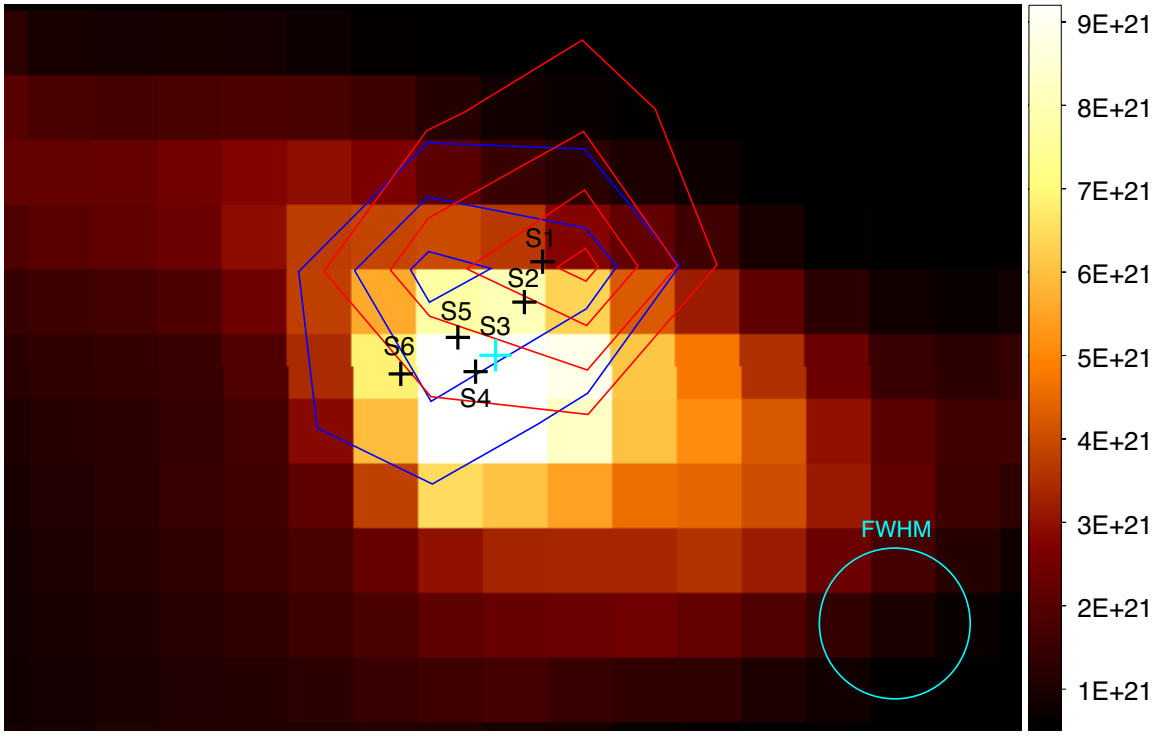

Figure 16. Contour maps of the blue- and red-shifted emission overlaid on the H_2 column density map. The blue solid contours show the blueshifted emission of $v_{LSR} = -45.72$ to -41.06 km s^{-1}. The red solid contours show the redshifted emission of $v_{LSR} = -34.71$ to -30.05 km s^{-1}. The lowest contour is 3 σ level (= 2.8 K km s^{-1} in T_A^*), and the contour interval is 3 σ. The crosses show the positions of S1 to S6. The JCMT beam size of 14″ is shown in the lower right corner.

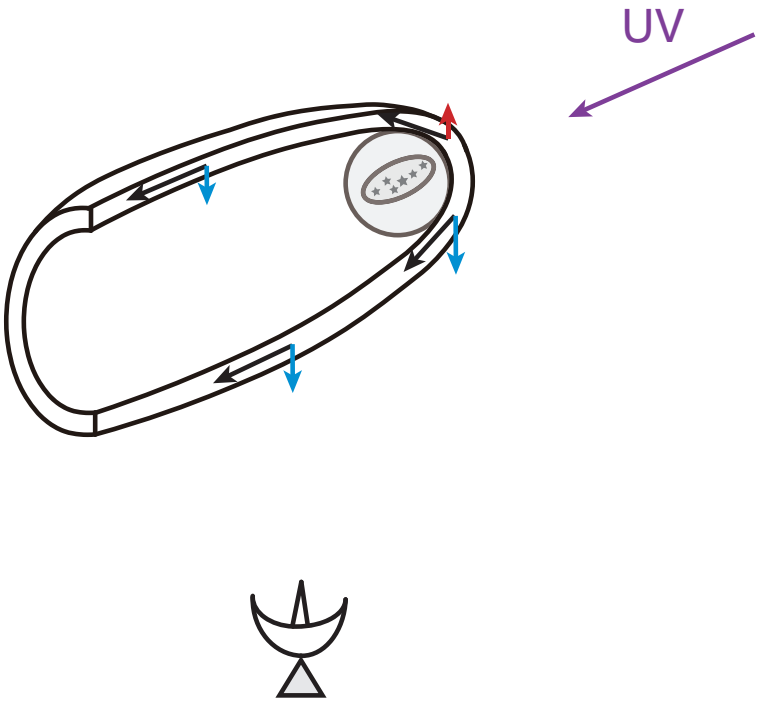

Figure 17. Schematic cross-section view of SFO 12. The gas radiatively accelerated is blown off from the cloud head toward the near side. The blue and red arrows, respectively, show the blue and red-shifted velocity components of the accelerated gas.

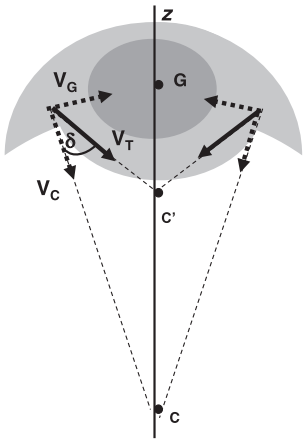

Figure 18. Schematic drawing from Figure 5 of Miao et al. (2009).

Table 1. Photometry Results with UH88 for the Cluster Members

Object	α (J2000)	δ (J2000)	J	H	K_s	Aperture rad.	Av	2MASS ID
			[mag]	[mag]	[mag]	[″]	[mag]	
(1)	(2)	(3)	(4)	(5)	(6)	(7)	(8)	(9)
S1	$2^h55^m01\overset{s}{.}36$	$+60°35'50\overset{''}{.}25$	16.83 ± 0.04	15.44 ± 0.05	14.75 ± 0.07	1.89	6.9	02550133+6035501
S2	$2^h55^m01\overset{s}{.}59$	$+60°35'46\overset{''}{.}53$	17.50 ± 0.06	15.83 ± 0.05	14.79 ± 0.07	1.89	9.5	02550158+6035465
S3	$2^h55^m01\overset{s}{.}97$	$+60°35'41\overset{''}{.}64$	17.16 ± 0.04	14.54 ± 0.05	12.37 ± 0.07	0.94	19.3	02550198+6035416
S4	$2^h55^m02\overset{s}{.}22$	$+60°35'40\overset{''}{.}15$	17.73 ± 0.05	16.53 ± 0.05	15.10 ± 0.07	0.94	>4.5	—
S5	$2^h55^m02\overset{s}{.}44$	$+60°35'43\overset{''}{.}36$	16.05 ± 0.04	14.71 ± 0.05	14.00 ± 0.07	0.94	6.7	—
S6	$2^h55^m03\overset{s}{.}17$	$+60°35'40\overset{''}{.}06$	16.57 ± 0.04	14.93 ± 0.05	13.94 ± 0.07	0.94	9.0	02550316+6035399

Table 2. Photometry Results with Subaru and SEIP Catalog Data for the Cluster Members

Object	H^a [mag]	K^a [mag]	L'^a [mag]	3.6 μm^b [mJy]	4.5 μm^b [mJy]	5.8 μm^b [mJy]	8.0 μm^b [mJy]
S1	16.78 ± 0.09	16.59 ± 0.02	<16.1	—	—	—	—
S2a	17.54 ± 0.09	18.12 ± 0.02	<14.6	—	—	—	—
S2b	17.70 ± 0.09	17.51 ± 0.02	″	—	—	—	—
S3a	—	—	9.01 ± 0.15	53.29 ± 0.015	82.90 ± 0.019	135.1 ± 0.06	—
S3b	20.4	16.2	—	—	—	—	—
S4	17.25 ± 0.09	16.66 ± 0.02	11.96 ± 0.15	—	—	—	—
S5	14.31 ± 0.09	13.81 ± 0.02	12.88 ± 0.15	—	—	—	—
S6	14.87 ± 0.09	14.21 ± 0.02	12.63 ± 0.15	2.787 ± 0.0035	3.798 ± 0.0041	5.456 ± 0.012	—

NOTE—In addition to the mid-infrared fluxes of Spitzer in this table, the WISE fluxes, 52.0 ± 1.1 mJy at 3.4 μm, 110.3 ± 1.9 mJy at 4.6 μ, 326.6 ± 4.5 mJy at 12μm, 1237.0 ± 25.1 mJy at 22μm, are also available for S3 in the source list of SEIP[b]. These fluxes might include those of the other cluster members due to the relatively lower angular resolution of WISE, $6\farcs1 - 12\farcs0$ (Wright et al. 2010), but they might come mostly from S3, considering its L' magnitude that is much larger than those of the other cluster members.

[a] The UKIRT faint standard stars were used for photometric calibration. The aperture radii are $0\farcs37$ at H, $0\farcs25$ at K, and $0\farcs21$ at L'.

[b] The source list of SEIP (Spitzer Enhanced Imaging Products; http://irsa.ipac.caltech.edu/cgi-bin/Gator/nph-dd) provides the aperture photometry fluxes ($3\farcs8$ diam.).

Table 3. YSO Candidates selected with UH88

ID #	α (J2000)	δ (J2000)	i' [mag]	J [mag]	H [mag]	K_s [mag]	Remarks
1	$2^h54^m54\overset{s}{.}50$	$+60°34'59\overset{''}{.}92$	20.34 ± 0.03	16.77 ± 0.04	15.76 ± 0.04	14.96 ± 0.04	10397[a], BRC12-8[b]
2	$2^h54^m54\overset{s}{.}34$	$+60°35'30\overset{''}{.}94$	22.23 ± 0.08	18.91 ± 0.06	18.01 ± 0.06	17.41 ± 0.06	this work
3	$2^h54^m53\overset{s}{.}59$	$+60°37'15\overset{''}{.}67$	20.60 ± 0.03	16.74 ± 0.04	15.99 ± 0.04	15.48 ± 0.04	10372[a], 02545360+6037156[c]

NOTE—[a]ID number in Table 2 of Koenig et al. (2008)

[b]ID number in Table 4 of Ikeda et al. (2008)

[c]2MASS ID number

ALL AUTHORS AND AFFILIATIONS

Rieko Imai [1], Koji Sugitani [1], Jingqi Miao [2], Naoya Fukuda [3], Makoto Watanabe [3, 4],

Takayoshi Kusune [1],

And

Andrew J. Pickles [5].

[1]Graduate School of Natural Sciences, Nagoya City University, Mizuho-ku, Nagoya 467-8501, Japan,

[2]School of Physical Sciences, University of Kent, Canterbury, Kent CT2 7NR, UK,

[3]Okayama University of Science, 1-1 Ridai-chou, Kita-ku, Okayama 700-0005, Japan,

[4]Subaru Telescope, National Astronomical Observatory of Japan, 650 North A'ohoku Place, Hilo, HI 96720, USA,

[5]Las Cumbres Observatory, Goleta, CA 93117, USA